NANO · MICRO small
www.small-journal.com

Erbium Single Atom Composite Photocatalysts for Reduction of CO_2 under Visible Light: CO_2 Molecular Activation and 4*f* Levels as an Electron Transport Bridge

Zhendong Han, Yue Zhao, Guoyang Gao, Wanying Zhang, Yang Qu, Hongyang Zhu, Peifen Zhu, and Guofeng Wang**

It is still challenging to design a stable and efficient catalyst for visible-light CO_2 reduction. Here, Er^{3+} single atom composite photocatalysts are successfully constructed based on both the special role of Er^{3+} and the special advantages of Zn_2GeO_4/g-C_3N_4 heterojunction in the photocatalysis reduction of CO_2. Especially, Zn_2GeO_4:Er^{3+}/g-C_3N_4 obtained by in situ synthesis is not only more conducive to the tight junction of Zn_2GeO_4 and g-C_3N_4, but also more favorable for g-C_3N_4 to anchor rare-earth atoms. Under visible-light irradiation, Zn_2GeO_4:Er^{3+}/g-C_3N_4 shows more than five times enhancement in the catalytic efficiency compared to that of pure g-C_3N_4 without any sacrificial agent in the photocatalytic reaction system. A series of theoretical and experimental results show that the charge density around Er, Ge, Zn, and O increases compared with Zn_2GeO_4:Er^{3+}, while the charge density around C decreases compared with g-C_3N_4. These results show that an efficient way of electron transfer is provided to promote charge separation, and the dual functions of CO_2 molecular activation of Er^{3+} single atom and 4*f* levels as electron transport bridge are fully exploited. The pattern of combining single-atom catalysis and heterojunction opens up new methods for enhancing photocatalytic activity.

1. Introduction

With the development of industrialization, excessive energy consumption and carbon dioxide (CO_2) emissions exacerbate the energy crisis and environmental pollution.[1–6] It is a serious problem for all countries in the world to explore a stable total amount control scheme of atmospheric CO_2 and actively deal with the energy crisis. It is expected to achieve a carbon-neutral cycle and alleviate the greenhouse effect and energy crisis by transforming CO_2 into available chemical fuel through solar photocatalytic technology.[7–15] Most of the existing photocatalysts are difficult to fully absorb and utilize visible light. Besides, the potentials at the band edge positions are difficult to meet the potential requirements of photocatalytic reaction at the same time, and the photogenerated carrier separation is poor.[16–19] Thus, the key technology bottlenecks of photocatalytic CO_2 reduction are the poor charge separation and low efficiency of photocatalyst during the photocatalytic reaction.[20–23] Combining two semiconductors with different bandgap energy can realize the complementary advantages of the two materials, which is an effective approach to improving photocatalytic efficiency.[24–27]

As a kind of semiconductor polymer photocatalyst, graphite carbon nitride (g-C_3N_4) has drawn extensive attention as it has suitable bandgap energy to absorb visible light, good stability, easy preparation, low cost, and non-toxic.[28,29] The bandgap of g-C_3N_4 is ≈2.7 eV, and the conduction band (CB) level is relatively negative, which promotes the reduction capability of photogenerated electrons.[30–35] However, g-C_3N_4 mainly absorbs the shorter wavelengths of light between 400 and 475 nm, and barely absorbs long-wavelength visible light a. The low specific surface area of g-C_3N_4, as well as the high recombination rate of photogenerated carriers, is another barrier that needs to be overcome.[36–38] Therefore, it is urgent to enhance the photogenerated charge separation rate and increase the carrier lifetime of g-C_3N_4. Coupling with other materials to promote electron-hole separation is one of the most effective approaches to improving photocatalytic performance.[39–41]

Zn_2GeO_4 is widely used in photocatalysis, electrochemical sensors, and lithium-ion batteries due to the advantages of high chemical stability, thermal stability, and light stability.[42–44] However, Zn_2GeO_4 also has the disadvantages of the wide bandgap, weak light adsorption, and low CO_2 adsorption. Fortunately, it is expected to promote the charge separation and

Z. Han, Y. Zhao, G. Gao, W. Zhang, Prof. Y. Qu, Prof. G. Wang
Key Laboratory of Functional Inorganic Material Chemistry
Ministry of Education
School of Chemistry and Materials Science
Heilongjiang University
Harbin 150080, China
E-mail: 2010070@hlju.edu.cn
Prof. H. Zhu
School of Physics and Electronic Engineering
Linyi University
Linyi 276005, P. R. China
E-mail: zhuhongyang@lyu.edu.cn
Prof. P. Zhu
Department of Physics and Engineering Physics
The University of Tulsa
Tulsa, OK 74104, USA
The ORCID identification number(s) for the author(s) of this article can be found under https://doi.org/10.1002/smll.202102089.

DOI: 10.1002/smll.202102089

improve the visible light photocatalytic activity of g-C_3N_4 by the combination of Zn_2GeO_4 and g-C_3N_4. The interface microstructure and bonding mode of composites have a great influence on the interface photogenerated charge transfer efficiency. Therefore, it is also expected to further improve the interface transport and enhance the photocatalytic efficiency by reasonably designing the interface microstructure.[45]

It is well known that rare-earth elements show a broad application prospect in the photocatalysis field due to their unique electronic structure and optical properties. The traditional view is that rare-earth ions play the role of forming impurity energy levels, adjusting energy band structure, and light conversion, that is, the luminescence of rare-earth ions can be further absorbed by semiconductor catalysts to fully utilize the light.[46–48] However, it is impossible to greatly improve the catalytic performance of the materials due to the low luminescent efficiency of rare-earth ions. With the advent of the era of single-atom catalysis, rare-earth single-atom catalysts are gradually emerging in the field of photocatalysis.[49] Reducing rare-earth nanomaterials to a single-atom scale, the unique structural characteristics of the rare-earth single atom might give them different or unexpected properties from the nanoscale homologs, which provides a new opportunity for efficient photocatalytic CO_2 reduction.[50,51]

Here, erbium (Er) single atom composite photocatalysts were successfully constructed by in situ synthesis and chemisorption, respectively. Especially, Zn_2GeO_4:Er^{3+}/g-C_3N_4 obtained by in situ synthesis is not only more conducive to the tight junction of Zn_2GeO_4:Er^{3+} and g-C_3N_4, but also more favorable for g-C_3N_4 to anchor rare-earth atoms. Under visible-light irradiation, the catalytic performance of Zn_2GeO_4:Er^{3+}/g-C_3N_4 is more than five times higher than that of pure g-C_3N_4. A series of theoretical and experimental results show that Er^{3+} single atoms play a dual role in CO_2 molecular activation and 4f levels as energy transfer bridge.

2. Results and Discussion

2.1. Synthesis Diagrams and the Proposed Mechanism Diagram of Photocatalysis

The erbium single atom composite catalysts were synthesized by in situ synthesis and chemisorption, respectively (**Scheme 1**). The synthesis parameters and name abbreviation of the samples are shown in Tables S1–S3, Supporting Information, in the ESI (electronic Supporting Information). g-C_3N_4 was obtained by calcining urea in a tubular furnace under the protection of nitrogen. Zn_2GeO_4 (or Zn_2GeO_4:Er^{3+}) was synthesized by the solvothermal reaction method. For the in situ synthesis of Zn_2GeO_4:Er^{3+}/g-C_3N_4, some g-C_3N_4 and the related reactants/solvents for Zn_2GeO_4:Er^{3+} synthesis was added into the reactor in a certain order for the solvothermal reaction. According to the ratio of Zn_2GeO_4:Er^{3+} to g-C_3N_4, these samples are named 7-ZGOE/CN-SS, 20-ZGOE/CN-SS, 60-ZGOE/CN-SS, 70-ZGOE/CN-SS, and 80-ZGOE/CN-SS. For the chemical adsorption synthesis, Zn_2GeO_4:Er^{3+}/g-C_3N_4 was obtained by mixing Zn_2GeO_4:Er^{3+} and g-C_3N_4 in methanol solution with an ultrasonic wave and then drying them under a nitrogen atmosphere. According to the ratio of Zn_2GeO_4:Er^{3+} and g-C_3N_4, these samples are named 5-ZGOE/CN-CM, 10-ZGOE/CN-CM, and 15-ZGOE/CN-CM.

The photoreduction process of the CO_2 under visible light irradiation and the proposed mechanism diagram of photocatalysis is also shown in Scheme 1. Here, the single-atom Er^{3+} not only was used to modify Zn_2GeO_4:Er^{3+} but also was introduced as the bridge of interfacial electron transfer for Zn_2GeO_4:Er^{3+} and g-C_3N_4, and thus enhanced the photocatalytic activity of CO_2 reduction. It is noted that not all RE ions are suitable for charge transfer bridges because the role of RE ions is not only related to the structure of RE ions but also related to the properties of Zn_2GeO_4:Er^{3+} and g-C_3N_4. The

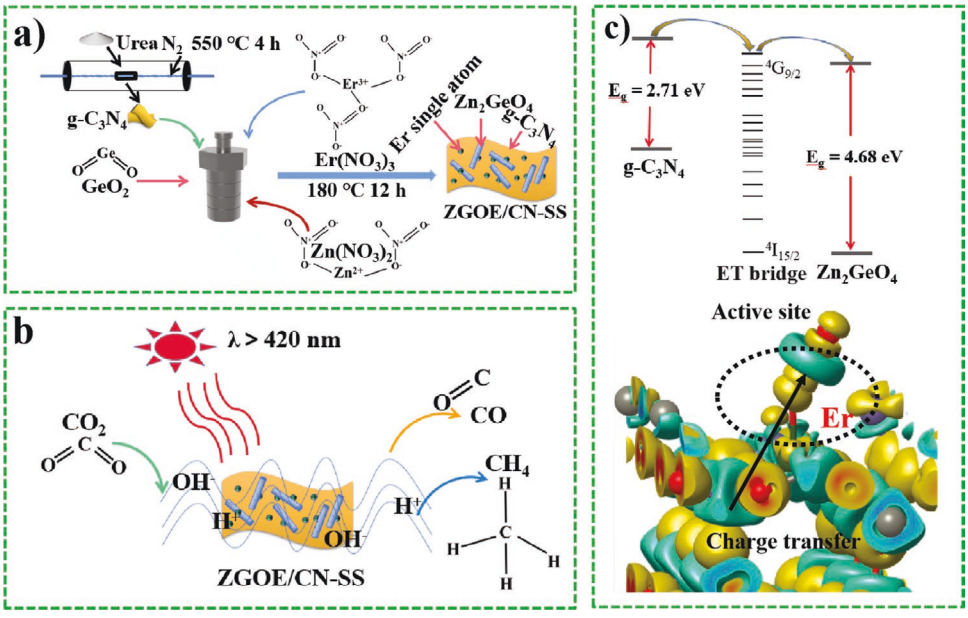

Scheme 1. a) Synthesis diagrams of g-C_3N_4 and ZGOE/CN-SS. b) The photoreduction of CO_2 process under visible light irradiation. c) The proposed mechanism diagram of photocatalysis.

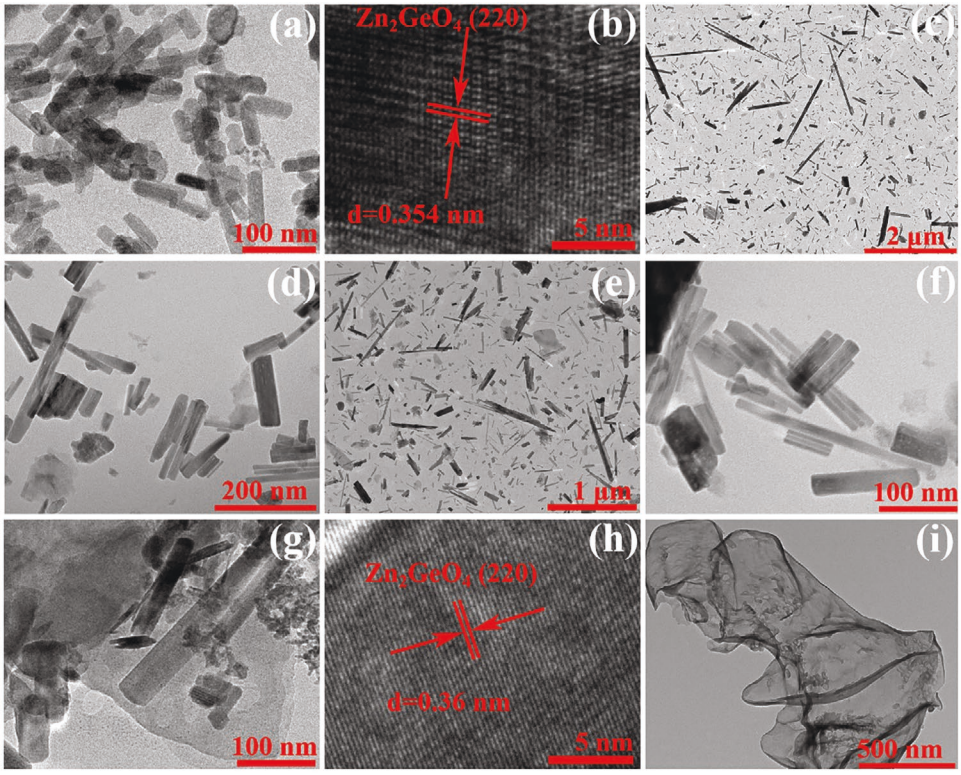

Figure 1. TEM and HRTEM images of a,b) ZGO:1Er, c,d) ZGO-L, e,f) ZGO:1Er-L, g,h) 70-ZGOE/CN-SS, and i) CN.

energy level of Er^{3+} is located between the conduction bands of Zn_2GeO_4:Er^{3+} and g-C_3N_4, so it is very suitable for electron transport. It is well known that tight junctions are essential for effective charge transfer in heterojunction nanocomposites. Here, Zn_2GeO_4:Er^{3+}/g-C_3N_4 obtained by in situ synthesis is not only more conducive to the tight junction of Zn_2GeO_4:Er^{3+} and g-C_3N_4, but also more favorable for g-C_3N_4 to anchor rare-earth atoms, which will be discussed later.

2.2. Morphology and Structure Analysis

The TEM, HRTEM, and SEM images of samples are shown in **Figure 1** and Figures S1 and S2, Supporting Information, in the ESI. A small amount of Er^{3+} doping has little effect on the morphology of Zn_2GeO_4:Er^{3+}. The morphology of Zn_2GeO_4:Er^{3+} or Zn_2GeO_4 looks like a flower cluster, which is mainly composed of rods. The effect of reaction time on the morphology of the sample shows that the longer the reaction time is, the longer the length of the rod is. The lattice fringes at a distance of 0.354 nm in the HRTEM image of ZGO:1Er between planes are attributed to the (220) crystal plane. For the 70-ZGOE/CN-SS sample, not only the sheet structure of g-C_3N_4 can be observed, but also ZGO:1Er can be attached to the surface of g-C_3N_4. The lattice fringes at a distance of 0.36 nm between planes for the HRTEM image of 70-ZGOE/CN-SS are attributed to the (220) crystal plane of ZGO:1Er. The results of the TEM images of 1-ZGOE/CN-CM, 10-ZGOE/CN-CM, and 15-ZGOE/CN-CM indicated that ZGO:1Er can be also attached to the surface of g-C_3N_4 by the chemisorption method.

To further confirm the dispersion state of Er elements, aberration-corrected HAADF-STEM (AC HAADF-STEM) measurement was carried out (**Figure 2**). The AC HAADF-STEM image clearly distinguishes the isolated bright spots from the matrix of 70-ZGOE/CN-SS, indicating that Er elements diffuse in 70-ZGOE/CN-SS in the form of atoms. This is because the 70-ZGOE/CN-SS synthesized in situ is more favorable for g-C_3N_4 to anchor rare-earth atoms. Energy dispersive spectroscopy (EDS) mapping shows that C, N, Ge, O, Zn, and Er elements are distributed throughout the composite as expected.

The phase structure of samples was confirmed by the X-ray diffraction (XRD) patterns (**Figure 3**a–c). The crystal phase of the prepared ZGO and ZGO:1Er^{3+} is a rhombohedral phase and the diffraction peaks are consistent with rhombohedral phase zinc germanate (JCPDS No. 11–0687). No obvious diffraction peaks related to Er^{3+} were detected, which indicates that the atomic-level dopant does not form a crystalline segregated dual-phase, and is well combined with the ZGO lattice. For ZGOE/CN-SS samples, no obvious diffraction peaks of CN were observed due to the high content and good crystallinity of ZGO:1Er^{3+}. It is noted that the total amount of reaction solvent is fixed, and thus, the diffraction peak of $Zn(NO_3)_2 \cdot 6H_2O$ and GeO_2 appears with the increase of CN content because the initial reactants cannot fully react. While for ZGOE/CN-CM obtained by the chemisorption method, the XRD diffraction peaks of both CN and ZGO:1Er^{3+} were observed.

The UV–vis absorption spectra of samples show that the absorption range broadens to the longer wavelength direction with the increase of CN content (Figure 3d). When the concentration of Er^{3+} is high enough, the characteristic absorption

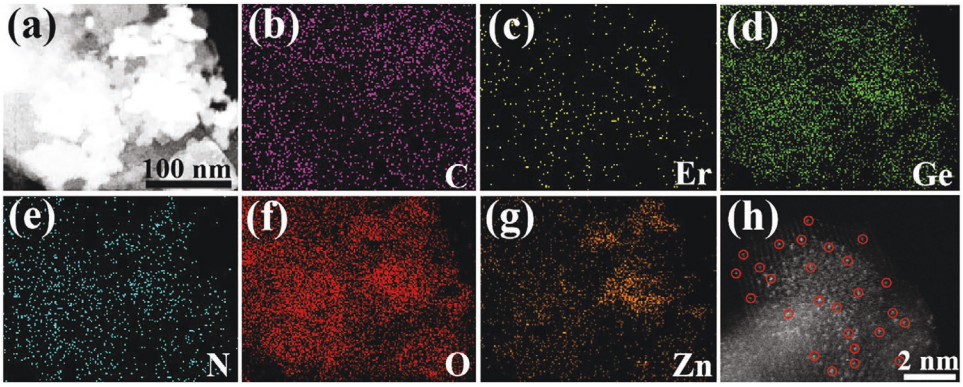

Figure 2. HAADF-STEM image and EDX elemental mappings of 70-ZGOE/CN-SS.

peaks of Er^{3+} were observed. Fourier transform infrared spectroscopy spectra are shown in Figure S3, Supporting Information, in the ESI. The two peaks at ≈532 and ≈840 cm^{-1} belong to the vibration modes of ZnO_4 and GeO_4 tetrahedral in ZGO, respectively. The bands at 1200–1700 cm^{-1} are mainly attributed to the vibration of the typical extended C-N heterocyclic ring, and the broadband at about 3500 cm^{-1} is attributed to the O—H tensile vibration of the sample surface. The intensity of the C—N band of the nanocomposite increases with the CN content.

The results of the nitrogen adsorption and desorption isotherms and corresponding pore size distributions calculated by the BJH method (Figure 3e and Figure S4, Supporting Information, in the ESI) indicated that the Brunauer–Emmett–Teller (BET) surface areas are 23.45, 31.13, 35.83, 30.25, and 50.68 $m^2\ g^{-1}$, for ZGO, ZGO:1Er, ZGO:2Er, CN, and 70-ZGOE/CN-SS, respectively. The hysteresis loops belong to the second type of isotherm, indicating that the samples have a large pore. Besides, the BET surface areas increase with the Er^{3+} concentration. Especially, the BET surface of 70-ZGOE/CN-SS is as high as 50 $m^2\ g^{-1}$. Generally speaking, the larger surface area is conducive to the adsorption of CO_2 molecules, thus improving the photocatalytic performance. The results of EDS indicated that Zn, Ge, O, and Er elements were observed in ZGO:1Er^{3+}. The Zn, Ge, O, C, and N elements can be observed in the EDS of 70-ZGOE/CN-SS, proving the formation of g-C_3N_4/Zn_2GeO_4:Er^{3+} nanocomposites.

Figure 4 shows the high-resolution XPS spectra of different samples. In the XPS spectra of C 1s (Figure 3a), the peaks at

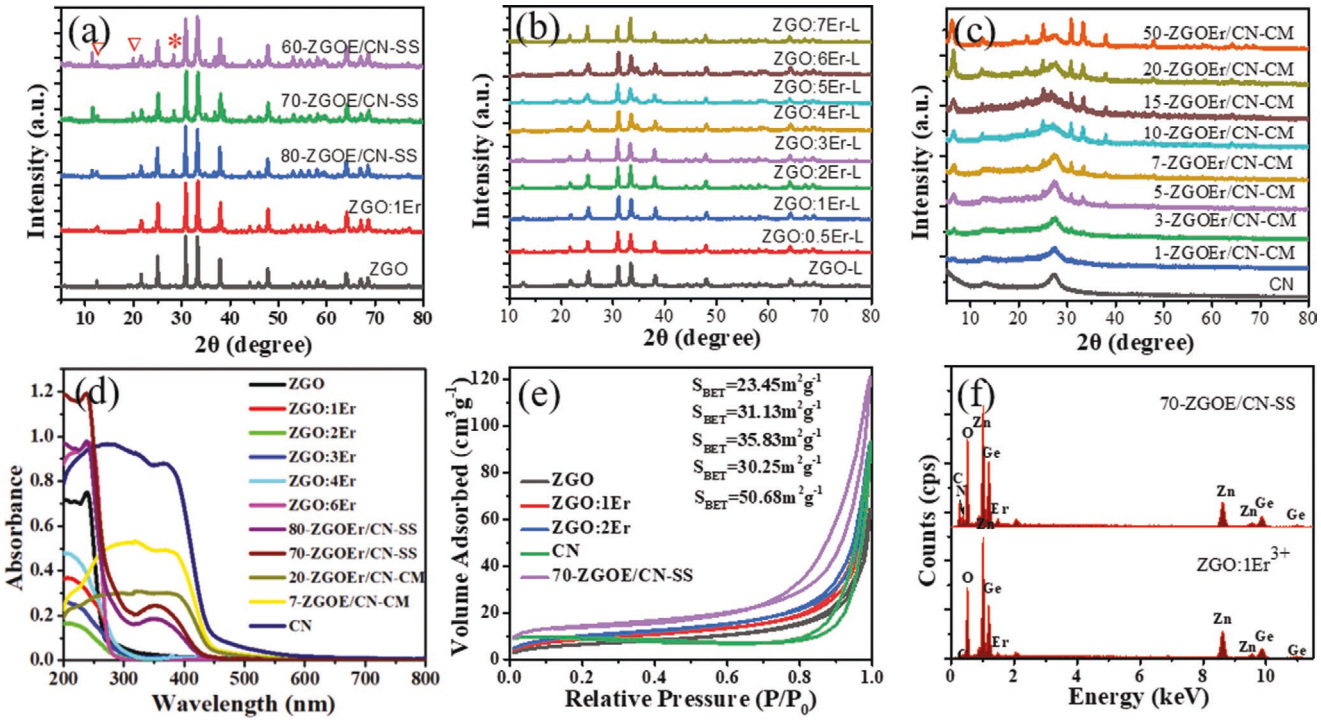

Figure 3. a–c) XRD patterns of ZGO, ZGO:1Er^{3+}, ZGOE/CN-SS, ZGOE/CN-CM, and CN. d) UV–vis absorption spectra of ZGO, ZGO:Er^{3+}, ZGOE/CN-SS, ZGOE/CN-CM, and CN. e) N_2 adsorption–desorption isotherm curves of ZGO, ZGO:Er^{3+}, ZGOE/CN-SS, and CN. f) EDS of ZGO:1Er^{3+} and 70-ZGOE/CN-SS.

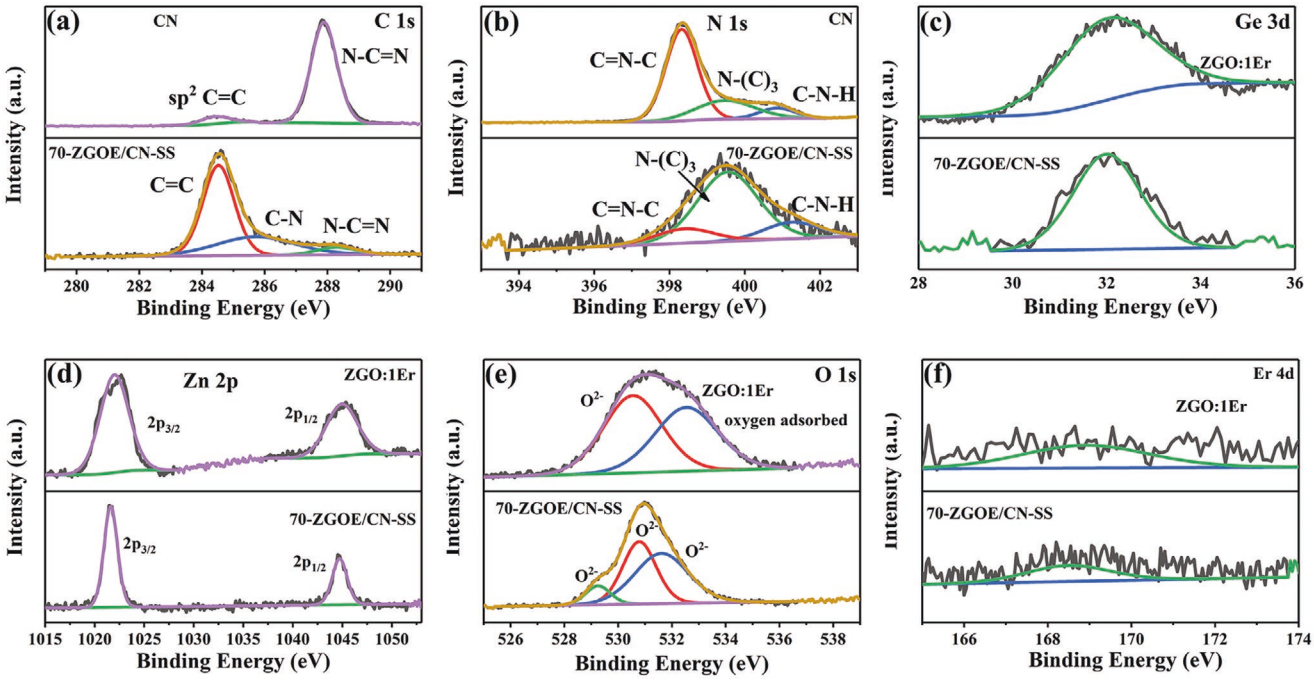

Figure 4. XPS spectra of different samples: a) C 1s, b) N 1s, c) Ge 3d, d) Zn 2p, e) O 1s, and f) Er 4d.

284.5 and 287.8 eV in the CN sample are attributed to the sp^2 C=C bond and the triazine-based N = C—N bond, respectively. A new peak at ≈285.8 eV of 70-ZGOE/CN-SS is attributed to the C—N bond. Compared with CN, the position of the N = C—N bond in 70-ZGOE/CN-SS moves toward high energy, indicating that the charge density around C decreases gradually. This result further proves that there is electron transfer from CN to ZGO:1Er in 70-ZGOE/CN-SS composites. In the XPS spectra of N 1s (Figure 3b), the peaks at ≈398.4, ≈399.5, and 400.9 eV of CN belong to sp^2-hybrid nitrogen (C = N—C), tertiary nitrogen group (N—$(C)_3$), and amino-functional group (C—N—H), respectively.

In the XPS spectra of Ge 3d, ZGO:1Er^{3+}, and 70-ZGOE/CN-SS samples, the peak of Ge 3d can be observed. In the XPS spectra of Zn 2p of the ZGO:1Er^{3+} sample, the two peaks at ≈1022.0 and ≈1045.1 eV are contributed to Zn $2p_{3/2}$ and Zn $2p_{1/2}$, respectively. In the XPS spectrum of O 1s, the two peaks at ≈530.5 and ≈532.5 eV are attributed to O^{2-} and oxygen adsorbed on the surface of ZGO:1Er^{3+}, including chemically adsorbed oxygen species or —OH groups. On the whole, it is surprised that the positions of all the Er 4d, Ge 3d, Zn 2p, and O 1s peaks in 70-ZGOE/CN-SS moves toward lower energy compared with ZGO:1Er^{3+}, indicating that the charge density around Er, Ge, Zn, and O increases gradually. On the contrary, the charge density around C decreases compared with CN. These results further prove that the 4f level of Er^{3+} ions can be used as a bridge for electron transport from CN to ZGO:1Er^{3+}, which can be further proved by the theoretical calculation results discussed later.

2.3. Photocatalytic Activity

The photocatalytic production amount for ZGO:*x*Er was monitored under UV light for 6 h, as shown in **Figure 5**a and Table S1, Supporting Information, in the ESI. The amounts of CO and CH_4 of pure ZGO are 25 and 5.4 μmol g^{-1} h^{-1}, respectively. When the concentration of Er^{3+} is 1mol%, the catalytic performance is the best (48 and 10 μmol g^{-1} h^{-1} for CO and CH_4). Besides, the hydrothermal time has little effect on the photocatalytic performance of the samples. The photocatalytic production amount for ZGOE/CN-SS and ZGOE/CN-CM was monitored under visible light for 6 h, as shown in Figure 5 and Tables S2 and S3, Supporting Information, in the ESI. The results showed that the 70-ZGOE/CN-SS sample shows the best photocatalytic activity, and the amounts of CO and CH_4 of 70-ZGOE/CN-SS is 6.3 and 10.4 μmol g^{-1} h^{-1}, which is much higher than those of CN samples (3 and 2 μmol g^{-1} h^{-1} for the amounts of CO and CH_4). For the ZGOE/CN-CM samples prepared by the chemisorption method, the 10-ZGOE/CN-CM shows the best photocatalytic activity, and the amounts of CO and CH_4 of 10-ZGOE/CN-CM is 4.8 and 7.2 μmol g^{-1} h^{-1}. Besides, the photocatalytic activity of 70-ZGOE/CN-SS is very stable (Figure 5d). The performance comparison of the rare earth single atom photocatalysts reported is summarized in **Table 1**. It is noted that the yield of CH_4 is more important than that of CO during the process of CO_2RR, so the performance of 70-ZGOE/CN-SS in this work is quite good. Of course, it is noted that not all RE ions are suitable for charge transfer bridges because the role of RE ions is not only related to the structure of RE ions but also related to the properties of ZGO and CN. So, there is still a lot of room for improvement in the design of RE single atom composite photocatalysts.

Figure 6a shows the photocurrent-time curves of CN and 70-ZGOE/CN-SS under visible light irradiation. Compared with CN, 70-ZGOE/CN-SS exhibits significantly higher photocurrent, which shows that 70-ZGOE/CN-SS can generate more photon carriers and has an excellent visible photocatalytic

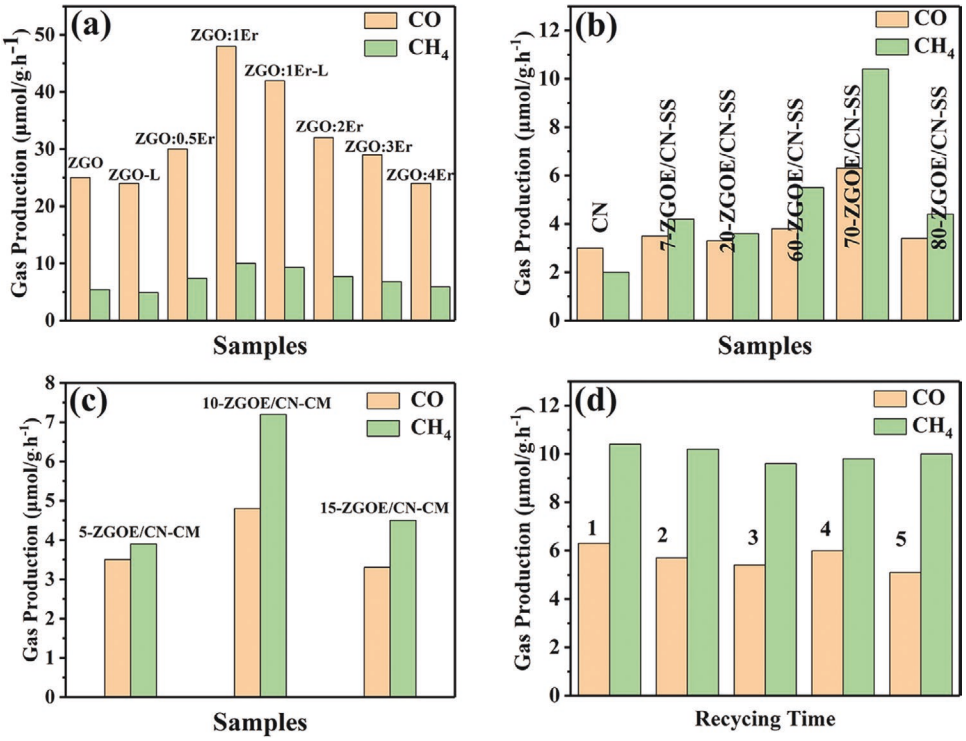

Figure 5. a) Production of CO and CH_4 for ZGO:*x*Er under UV light. b) Production of CO and CH_4 for CN and ZGOE/CN-SS under visible light. c) Production of CO and CH_4 for ZGOE/CN-CM under visible light. d) Stability of 70-ZGOE/CN-SS photocatalyst.

performance. The radius of the high-frequency semicircle of the impedance is related to the barrier of the interface charge transfer. The smaller the radius of the semicircle, the higher the efficiency of charge transfer. The results of the electrochemical impedance spectra indicated that the interface charge transfer rate of 70-ZGOE/CN-SS heterojunction is faster than that of g-C_3N_4 (Figure 6b). The coumarin was used as a fluorescent probe to measure the number of hydroxyl radicals produced under 390-nm light excitation, and the spectral signal of 70-ZGOE/CN-SS was larger than that of g-C_3N_4 (Figure 6c). The photoluminescence spectra of different samples indicated that the 70-ZGOE/CN-SS heterojunction is beneficial to charge transfer, inhibits the recombination of photogenerated carriers, and improves the photocatalytic performance of the materials. The Luminescence decay curves of g-C_3N_4 and 70-ZGOE/CN-SS obtained under 290 nm light excitation are shown in Figure 6e. The average fitting data of fluorescence lifetime of g-C_3N_4 and 70-ZGOE/CN-SS are 1.69 and 1.35 μs, respectively. It is noted that the emission of 70-ZGOE/CN-SS comes from g-C_3N_4, and thus, the shorter fluorescence lifetime of 70-ZGOE/CN-SS further proves the energy transfer from g-C_3N_4 to ZGO:1Er. The formation of heterojunction and Er^{3+} doping are beneficial to electron transport and preventing the recombination of electrons and holes. The PL spectra of ZGOE/CN-CM prepared by the chemisorption method are shown in Figure S5, Supporting Information, which further prove that the heterojunction material is conducive to charge transfer, thus improving the photocatalytic activity. The carrier density can be compared by comparing the slope of the Schottky model. The smaller the slope is, the higher the carrier density is. Both the slopes of Mott Schottky curves are positive, which indicates that the materials are *n*-type semiconductors (Figure 6f). 70-ZGOE/CN-SS has a smaller slope and higher carriers, which improves the performance of photocatalysis. To further confirm the source of the produced CH_4, we carried out an isotopic experiment using CO_2 under the identical photocatalytic reaction conditions. The photocatalytic evolution of CH_4 was analyzed by gas chromatography mass (GC-MS), of which the peak $m/z = 17$ is assigned to CH_4 and the fragment ion of CH_4 is seen, as well as, shown in Figure S6, Supporting Information, in the ESI.

Table 1. Comparison of visible-light photocatalytic performance for the rare earth single atom photocatalysts reported.

Single-atom photocatalysts	Sacrificial agent	Catalytic performance [μmol h^{-1} g^{-1}]		References
		CO	CH_4	
g-C_3N_4:Er	Without	47.1	2.5	[50]
g-C_3N_4:La	TEOA	92	5.6	[51]
Zn_2GeO_4:Er/g-C_3N_4	TEOA	6.3	10.4	This work

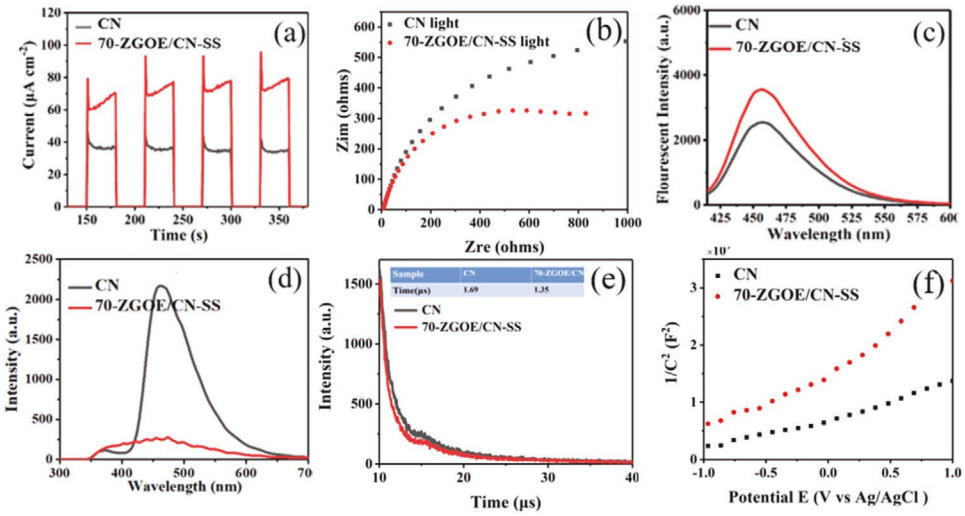

Figure 6. a) Photocurrent-time curves and b) electrochemical impedance spectroscopy (EIS) in the light of CN and 70-ZGOE/CN-SS. c) Fluorescence spectra related to the produced hydroxyl radicals of CN and 70-ZGOE/CN-SS under 390 nm light excitation. d) PL spectra of CN and 70-ZGOE/CN-SS under 290 nm excitation. e) Luminescence decay curves obtained under 290-nm light excitation. f) Mott–Schottky plots of CN and 70-ZGOE/CN-SS.

2.4. DFT Calculation

To further study the rationality of the designed charge separation system, DFT was used to select and optimize the appropriate lattice structures of g-C_3N_4, Zn_2GeO_4, and Zn_2GeO_4/g-C_3N_4 heterojunction (**Figure 7**). The calculated band gaps of g-C_3N_4 and Zn_2GeO_4 are about 3.0 and 4.21 eV, respectively, which are close to the experimental values. The calculated optical properties of g-C_3N_4 and Zn_2GeO_4 are shown in Figure S7, Supporting Information, in the ESI, indicating that Zn_2GeO_4/g-C_3N_4 heterojunction materials can take into account the properties of the two materials, therefore we can adjust the ratio of Zn_2GeO_4 to g-C_3N_4, to achieve our different purposes. More, the results of the calculated absorption spectra are consistent with those of the experimental UV–vis absorption spectra discussed above, which is conducive to the construction of composite materials and the improvement of photocatalytic activity.

The work functions of g-C_3N_4, Zn_2GeO_4, and Zn_2GeO_4/g-C_3N_4 were also calculated to further explore the charge transfer between g-C_3N_4 and Zn_2GeO_4. The work functions of g-C_3N_4 (001), Zn_2GeO_4 (001), and Zn_2GeO_4/g-C_3N_4 are 4.09, 6.66, and 4.25 eV, respectively. The g-C_3N_4 (001) surface has a higher Fermi level than the Zn_2GeO_4 (001) surface, and thus, the electrons will be transferred from g-C_3N_4 to Zn_2GeO_4 through the interface to line up Fermi level, and corresponding, a built-in electric field is formed between them when Zn_2GeO_4 is in contact with g-C_3N_4.

The optimized geometric structures and theoretical simulation results of the charge density of Zn_2GeO_4, Zn_2GeO_4:Er^{3+}, and g-C_3N_4 are shown in Figure S8, Supporting Information, in the ESI. The doping of Er^{3+} into Zn_2GeO_4 affected the bond strength at the interface between Zn_2GeO_4 and g-C_3N_4. Specifically, the Zn—N bond lengths in Zn_2GeO_4/g-C_3N_4 heterojunction are 2.12 and 2.14 Å; the Ge—N bond length in Zn_2GeO_4/g-C_3N_4 heterojunction is 2.06 Å; The Zn—N bond lengths in Zn_2GeO_4:Er^{3+}/g-C_3N_4 heterojunction are 2.23, 2.21, 2.21, 2.23, 209 Å; the Ge—N bond lengths in Zn_2GeO_4:Er^{3+}/g-C_3N_4 heterojunction are 2.07, 2.20, and 2.04 Å. There is an additional C-O bond formed in Zn_2GeO_4:Er^{3+}/g-C_3N_4 heterojunction and the bond length is 1.45 Å. Therefore, doping of Er into Zn_2GeO_4 not only can change the bond length but also can form the additional bond, indicating that the Er^{3+} ions on the surface of Zn_2GeO_4 are more conducive to the formation of heterojunction, as well as, the bridge of interface charge transfer.

The results of geometric structures and calculated adsorption energies (E_{ads}) of CO_2 on the $Zn_{12}Ge_6O_{24}$ (001) surface with different adsorption sites indicated that the E_{ads} of CO_2 is 2.819 eV when C and O of CO_2 bond with O and Zn of $Zn_{12}Ge_6O_{24}$, as shown in **Figure 8**. When O of CO_2 can bond with Zn of $Zn_{12}Ge_6O_{24}$, and the E_{ads} of CO_2 is 0.211 or 0.127 eV. The calculated E_{ads} of CO_2 on the surface of $C_{57}N_{76}$ (001) is 4.22 eV (Figure S9, Supporting Information, in the ESI). All the E_{ads} of CO_2 increase after doping Er^{3+} ions, which is beneficial to the photoreduction of CO_2.

To investigate the effect of Er^{3+} on the charge density difference in Zn_2GeO_4 and Zn_2GeO_4/g-C_3N_4 heterojunction, the charge density difference of Zn_2GeO_4 and Zn_2GeO_4/g-C_3N_4 before and after forming heterojunctions were also studied (Figure 8). The charge analysis showed that the replacement of Er with Zn affects the interactions between Zn, Ge, and O. Thus, the 4f levels of some Er^{3+} located at the interface between Zn_2GeO_4 and g-C_3N_4 acts as an electron transport bridge, and the rest of Er^{3+} were anchored by g-C_3N_4 during the in situ synthesis process, which not only can result in the change of the density of the surrounding electron cloud but also can better absorb CO_2 and play the role of activation center.

3. Conclusion

In summary, this study aims to start from selective control at atomic and molecular scales, combine the characteristics of a rare-earth single atom and the advantages of heterojunction, and prepare rare-earth single atom composite photocatalyst

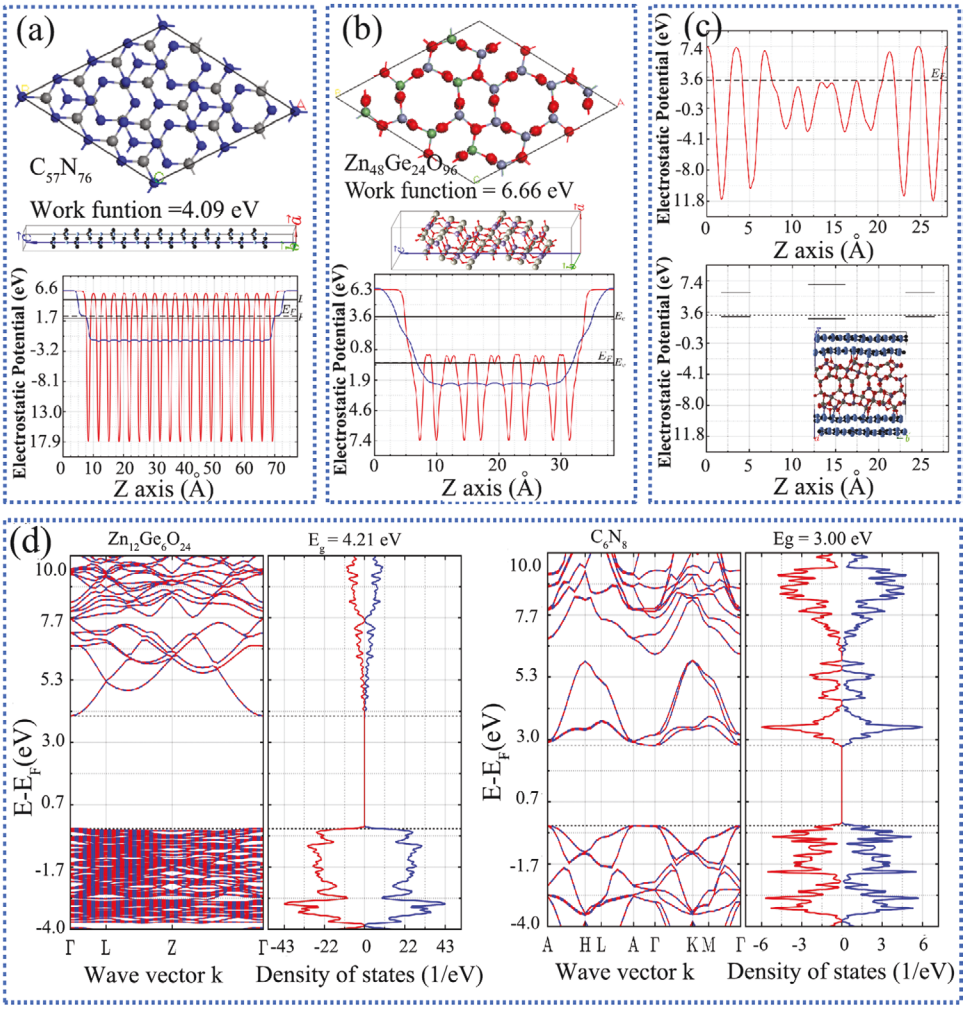

Figure 7. Geometric structures and calculated work functions of a–c) $C_{57}N_{76}$, $Zn_{12}Ge_6O_{24}$, and $C_{57}N_{76}/Zn_{12}Ge_6O_{24}$ heterojunction. d) Calculated band structure (BS) and density of states (DOS) of $Zn_{12}Ge_6O_{24}$ and g-C_3N_4.

through rare-earth single atom bridging g-C_3N_4 and Zn_2GeO_4, to provide an efficient way of electron transfer as well as promote charge separation. As we expected, Zn_2GeO_4:Er^{3+}/g-C_3N_4 obtained by the in situ synthesis is not only more conducive to the tight junction of Zn_2GeO_4 and g-C_3N_4, but also more favorable for g-C_3N_4 to anchor rare-earth atoms. Under visible-light irradiation, the catalytic efficiency of Zn_2GeO_4:Er^{3+}/g-C_3N_4 is nearly four times higher than that of pure g-C_3N_4. The results show that the charge density around C decreases compared with g-C_3N_4, while the charge density around Er, Ge, Zn, and O increases compared with Zn_2GeO_4:Er^{3+}, indicating that an efficient way of electron transfer from g-C_3N_4 to Zn_2GeO_4 was provided to promote charge separation. The 4*f* levels of some Er^{3+} single atom in the interface of g-C_3N_4 and Zn_2GeO_4 act as electron transport bridges, and the rest of Er^{3+} single atom anchored on the surface of g-C_3N_4 act as CO_2 molecular activation centers. It is expected that the results of this work can provide a great theoretical and experimental guidance for the rational design of RE single atom composite photocatalysts to adjust the bandgap and light capture ability, promote charge separation, and improve the visible light photocatalytic performance of materials.

4. Experimental Section

The chemicals, synthesis of Zn_2GeO_4: Er^{3+} and g-C_3N_4, and characterization details are shown in supporting information.

Synthesis of Zn_2GeO_4: Er^{3+}/g-C_3N_4 by the in situ synthesis (ZGOE/CN-SS). As mentioned above, the synthesis process of g-C_3N_4 is shown in supporting information. And then, a certain amount of g-C_3N_4 and $Zn(NO_3)_2{\cdot}6H_2O$ was put into a solution including 20 mL deionized water and 10 mL $N_2H_4{\cdot}H_2O$ under stirring until the solid was dissolved completely. Then, some GeO_2 was added to the above solution and fully stirred. The mixed solution was placed in a polytetrafluoroethylene autoclave and heated in an oven for 12 or 24 h. The autoclave was naturally cooled to room temperature, and the obtained product was washed five times with distilled water and ethanol, and finally dried in an oven at 60 °C for 8 h.

Synthesis of Zn_2GeO_4:Er^{3+}/g-C_3N_4 by the chemisorption method (ZGOE/CN-CM). As mentioned above, the g-C_3N_4 was obtained by annealing melamine at 550 °C for 2 h under an N_2 atmosphere followed

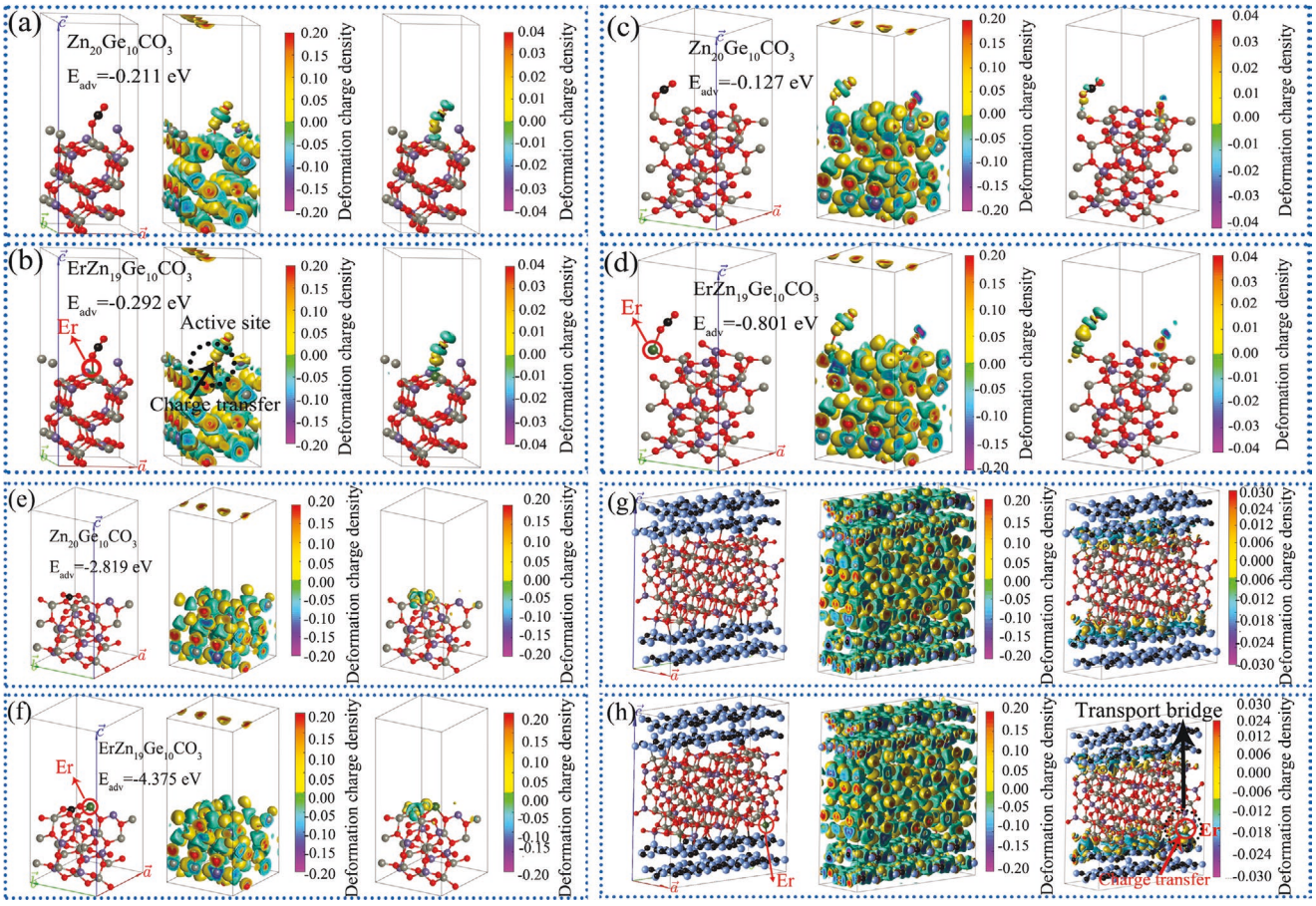

Figure 8. a–f) The effect Er^{3+} on the charge density difference in CO_2 adsorbed on the surface of $Zn_{12}Ge_6O_{24}$ with different adsorption sites. g,h) The effect of Er^{3+} on the charge density difference in $C_{57}N_{76}/Zn_{11}ErGe_6O_{24}$ heterojunctions.

by a grinding treatment for subsequent experiments. Then, a certain amount of g-C_3N_4 was added into methanol and put in an ultrasonic bath for 3 h to make g-C_3N_4 exfoliated completely. Then, different masses of Zn_2GeO_4:Er^{3+} were put into the above solution and kept ultrasonic for 30 min, finally stirred thoroughly until evaporated.

Supporting Information

Supporting Information is available from the Wiley Online Library or from the author.

Acknowledgements

This work was supported by the National Natural Science Foundation of China (No. 21871079 and 11774128) and the Natural Science Foundation of Shandong Province (ZR2018JL003, 2019KJJ003).

Conflict of Interest

The authors declare no conflict of interest.

Data Availability Statement

Research data are not shared.

Keywords

interfacial charge separation, single-atom Er^{3+}, visible-light photocatalysis, Zn_2GeO_4/g-C_3N_4

Received: April 10, 2021
Revised: April 30, 2021
Published online:

[1] W. Tu, Y. Zhou, Z. Zou, *Adv. Mater.* **2014**, *26*, 4607.
[2] Y. Zheng, A. Vasileff, X. Zhou, Y. Jiao, M. Jaroniec, S. Qiao, *J. Am. Chem. Soc.* **2019**, *141*, 7646.
[3] C. Song, X. Liu, M. Xu, D. Masi, Y. Wang, Y. Deng, M. Zhang, X. Qin, K. Feng, J. Yan, J. Leng, Z. Wang, Y. Xu, B. Yan, S. Jin, D. Xu, Z. Yin, D. Xiao, D. Ma, *ACS Catal.* **2020**, *10*, 10364.
[4] X. Li, Y. Sun, J. Xu, Y. Shao, J. Wu, X. Xu, Y. Pan, H. Ju, J. Zhu, Y. Xie, *Nat. Energy* **2019**, *4*, 690.
[5] J. Bian, J. Feng, Z. Zhang, Z. Li, Y. Zhang, Y. Liu, S. Ali, Y. Qu, L. Bai, J. Xie, D. Tang, X. Li, F. Bai, J. Tang, L. Jing, *Angew. Chem., Int. Ed.* **2019**, *58*, 10873.
[6] G. Zhao, W. Zhou, Y. Sun, X. Wang, H. Liu, X. Meng, K. Chang, J. Ye, *Appl. Catal., B* **2018**, *226*, 252.
[7] X. Zhao, Y. Fan, W. Zhang, X. Zhang, D. Han, L. Niu, A. Ivaska, *ACS Catal.* **2020**, *10*, 6367.
[8] F. Xu, K. Meng, B. Zhu, H. Liu, J. Xu, J. Yu, *Adv. Funct. Mater.* **2019**, *29*, 1904256.

[9] S. Wang, Y. Hou, X. Wang, *ACS Appl. Mater. Interfaces* **2015**, *7*, 4327.
[10] Q. Zhang, J. Joo, Z. Lu, M. Dahl, D. Oliveira, M. Ye, Y. Yin, *Nano Res.* **2010**, *4*, 103.
[11] S. Tian, M. Hu, Q. Xu, W. Gong, W. Chen, J. Yang, Y. Zhu, C. Chen, J. He, Q. Liu, H. Zhao, D. Wang, Y. Li, *Sci. China Mater.* **2020**, *64*, 642.
[12] X. Li, H. Rong, J. Zhang, D. Wang, Y. Li, *Nano Res.* **2020**, *13*, 1842.
[13] N. Fu, X. Liang, Z. Li, W. Chen, Y. Wang, L. Zheng, Q. Zhang, C. Chen, D. Wang, Q. Peng, L. Gu, Y. Li, *Nano Res.* **2020**, *13*, 947.
[14] K. Kamada, J. Jung, T. Wakabayashi, K. Sekizawa, S. Sato, T. Morikawa, S. Fukuzumi, S. Saito, *J. Am. Chem. Soc.* **2020**, *142*, 10261.
[15] H. Dong, X. Zhang, Y. Lu, Y. Yang, Y. Zhang, H. Tang, F. Zhang, Z. Yang, X. Sun, Y. Feng, *Appl. Catal., B* **2020**, *276*, 119173.
[16] J. Sun, J. Bian, J. Li, Z. Zhang, Z. Li, Y. Qu, L. Bai, Z.-D. Yang, L. Jing, *Appl. Catal., B* **2020**, *277*, 119199.
[17] F. Yang, Q. Zhang, J. Zhang, L. Zhang, M. Cao, W.-L. Dai, *Appl. Catal., B* **2020**, *278*, 119290.
[18] F. Raziq, J. He, J. Gan, M. Humayun, M. B. Faheem, A. Iqbal, A. Hayat, S. Fazal, J. Yi, Y. Zhao, K. Dhanabalan, X. Wu, A. Mavlonov, T. Ali, F. Hassan, X. Xiang, X. Zu, H. Shen, S. Li, L. Qiao, *Appl. Catal., B* **2020**, *270*, 118870.
[19] S. Chen, M. Shang, L. Wang, Z. Yang, F. Gao, J. Zheng, W. Yang, *ACS Appl. Mater. Interfaces* **2017**, *9*, 35178.
[20] J. Liao, W. Cui, J. Li, J. Sheng, H. Wang, X. Dong, P. Chen, G. Jiang, Z. Wang, F. Dong, *Chem. Eng. J.* **2020**, *379*, 122282.
[21] Y. Wang, Y. Tian, Z. Lang, W. Guan, L. Yan, *J. Mater. Chem. A* **2018**, *6*, 21056.
[22] Y. Li, S. Wang, W. Chang, L. Zhang, Z. Wu, R. Jin, Y. Xing, *Appl. Catal., B* **2020**, *274*, 119116.
[23] J. Bian, Y. Qu, X. Zhang, N. Sun, D. Tang, L. Jing, *J. Mater. Chem. A* **2018**, *6*, 11838.
[24] C. Chen, T. Wu, H. Wu, H. Liu, Q. Qian, Z. Liu, G. Yang, B. Han, *Chem. Sci.* **2018**, *9*, 8890.
[25] P. Zhang, S. Wang, B. Guan, X. Lou, *Energy Environ. Sci.* **2019**, *12*, 164.
[26] L. Cheng, Q. Xiang, Y. Liao, H. Zhang, *Energy Environ. Sci.* **2018**, *11*, 1362.
[27] H. She, H. Zhou, L. Li, Z. Zhao, M. Jiang, J. Huang, L. Wang, Q. Wang, *ACS Sustainable Chem. Eng.* **2018**, *7*, 650.
[28] J. Shen, Y. Li, H. Zhao, K. Pan, X. Li, Y. Qu, G. Wang, D. Wang, *Nano Res.* **2019**, *12*, 1931.
[29] H. Li, S. Gan, H. Wang, D. Han, L. Niu, *Adv. Mater.* **2015**, *27*, 6906.
[30] M. Zhou, S. Wang, P. Yang, C. Huang, X. Wang, *ACS Catal.* **2018**, *8*, 4928.
[31] X. Zhang, Z. Chen, Y. Feng, J. Qiu, J. Yao, *ACS Sustainable Chem. Eng.* **2017**, *6*, 1068.
[32] R. Hailili, D. Jacobs, L. Zang, C. Wang, *Appl. Surf. Sci.* **2018**, *456*, 360.
[33] D. Bagchi, V. Rathnam, P. Lemmens, I. Banerjee, S. Pal, *ACS Omega* **2018**, *3*, 10877.
[34] F. Shaik, I. Peer, P. K. Jain, L. Amirav, *Nano Lett.* **2018**, *18*, 4370.
[35] Q. Bi, J. Wang, J. Lv, J. Wang, W. Zhang, T. Lu, *ACS Catal.* **2018**, *8*, 11815.
[36] P. Cheung, S. Kapper, T. Zeng, M. Thompson, C. Kubiak, *J. Am. Chem. Soc.* **2019**, *141*, 14961.
[37] Y. Pan, Y. You, S. Xin, Y. Li, G. Fu, Z. Cui, Y. Men, F. Cao, S. Yu, J. Goodenough, *J. Am. Chem. Soc.* **2017**, *139*, 4123.
[38] D. Panayotov, A. Frenkel, J. Morris, *ACS Energy Lett.* **2017**, *2*, 1223.
[39] S. Bhosale, A. Kharade, E. Jokar, A. Fathi, S. Chang, E. Diau, *J. Am. Chem. Soc.* **2019**, *141*, 20434.
[40] Y. Xu, X. Jin, T. Ge, H. Xie, R. Sun, F. Su, X. Li, L. Ye, *Chem. Eng. J.* **2021**, *409*, 128178.
[41] S. Fu, X. Liu, J. Ran, Y. Jiao, S.-Z. Qiao, *Appl. Surf. Sci.* **2021**, *540*, 148293.
[42] J. Wang, Y. Asakura, S. Yin, *Nanoscale* **2019**, *11*, 20151.
[43] Z. Hou, X. Zou, X. Song, X. Pu, Y. Geng, L. Wang, *Int. J. Hydrogen Energy* **2019**, *44*, 28649.
[44] Y. Wang, Y. Li, X. Wang, A. Chen, H. Yang, *ChemPlusChem* **2017**, *82*, 199.
[45] Z. Zhuang, Q. Kang, D. Wang, Y. Li, *Nano Res.* **2020**, *13*, 1856.
[46] W. Chen, P. Liao, P. Jin, L. Zhang, B. Ling, S. Wang, Y. Chan, X. Chen, Y. Zheng, *J. Am. Chem. Soc.* **2020**, *142*, 4663.
[47] J. Wu, Y. Xie, Y. Ling, J. Si, X. Li, J. Wang, H. Ye, J. Zhao, S. Li, Q. Zhao, Y. Hou, *Chem. Eng. J.* **2020**, *400*, 125944.
[48] J. Shi, J. Ye, L. Ma, S. Ouyang, D. Jing, L. Guo, *Chem. - Eur. J.* **2012**, *18*, 7543.
[49] X. Ye, C. Yang, X. Pan, J. Ma, Y. Zhang, Y. Ren, X. Liu, L. Li, Y. Huang, *J. Am. Chem. Soc.* **2020**, *142*, 19001.
[50] S. Ji, Y. Qu, T. Wang, Y. Chen, G. Wang, X. Li, J. Dong, Q. Chen, W. Zhang, Z. Zhang, S. Liang, R. Yu, Y. Wang, D. Wang, Y. Li, *Angew. Chem., Int. Ed.* **2020**, *59*, 10651.
[51] P. Chen, B. Lei, X. Dong, H. Wang, J. Sheng, W. Cui, J. Li, Y. Sun, Z. Wang, F. Dong, *ACS Nano* **2020**, *14*, 15841.